Dynamic Control of Piezoelectricity Enhancement via Modulation of the Bulk Photovoltaic Effect in a BiFeO₃ Thin Film

Yooun Heo,* Hangbo Zhang, and Marin Alexe*

Piezoelectricity, which is an electromechanical effect induced by conversion between mechanical and electrical energy, is one of the key functionalities in ferroelectric oxides. Traditionally, structural engineering in synthesis via a variety of processing control parameters has been a well-established route to host so-called morphotropic phase boundaries for enhancing piezoelectricity. However, this involves dealing with synthetical complexity and difficulties of strictly controlling structures and defects. Instead, for simple and in situ control, here, a critical pathway for light-induced piezoelectricity enhancement and its dynamic control is unveiled in a BiFeO₃/DyScO₃ thin film by implementing an in-plane geometry operation, allowing for modulation of the bulk photovoltaic effect. A series of in-plane length-dependent piezoresponse force microscopy and conductive atomic force microscopy-based measurements under illumination reveals its strong influence on the photocurrent and photovoltage, consequently revealing a maximum of eightfold increase of the effective piezoelectric coefficient, d_{zz}. Light polarization dependent measurements show sinusoidal behavior of piezoelectricity closely linked to photocurrent variations, leading to a further threefold increase of d_{zz}. Temporal decay measurements reveal persistent behavior of enhanced piezoelectricity after removal of illumination, associated with reemission of photocarriers trapped in sub-levels. These results pave the way for light-induced piezoelectricity enhancement compatible with the photovoltaic effect in ferroelectric thin films for multifunctional nano-optoelectronics.

1. Introduction

Structural engineering in synthesis via chemical doping and epitaxial strain has been established as a robust control parameter for a variety of functionalities in oxide thin films.[1–6] One such

Y. Heo,[+] H. Zhang, M. Alexe
Department of Physics
University of Warwick
Coventry CV4 7AL, UK
E-mail: yooun.heo@mat.ethz.ch; m.alexe@warwick.ac.uk

The ORCID identification number(s) for the author(s) of this article can be found under https://doi.org/10.1002/aelm.202200785.

[+]Present address: Department of Materials, ETH Zurich, Zurich 8093, Switzerland

pronounced example is the strain-induced morphotropic phase boundary (MPB), serving as a key source for intriguing functionalities. In this regard, BiFeO₃ (BFO) has been considered a successful functional oxide with such MPB regions for largely enhanced electromechanical[7–9] and magnetoelectric coupling,[10,11] anisotropic conduction,[12,13] metal-insulator transitions,[14,15] photovoltaic effects,[16,17] and elastic softening.[18–20] Of all, the giant effective piezoelectric coefficient, d_{33} realized by phase boundary motion at the MPB, is particularly appealing for energy harvesting devices.[8] However, the prerequisite of synthesis to host MPB adds complexity, causing structural modification and thus resulting in rather an invasive way of enhancing piezoelectricity. Very recently, an alternative pathway of using light to induce a sevenfold enhancement of piezoelectricity was reported in a single crystal of BFO, offering simple and in situ control without altering its pristine structures.[21] The key factor is the bulk photovoltaic effect (BPV), resulting in generation of the open circuit voltage and photocarriers with their associated surface potential and doping density contributions respectively to piezoelectricity enhancement within the effective length of the bulk material. The BPV is only realized in non-centrosymmetric materials under illumination with higher energy than the bandgap, providing an essential source of significant electronic polarization, simulating the similar role as the p-n junction and Schottky barrier in conventional photovoltaics.[22,23] In addition to the symmetry requirement, material dimensions are also of critical importance for realization of the BPV. In case of thin films, however, the effective material length is the film thickness, typically ranging from 10's to 100's of nm, which is a limiting factor for sufficient realization of the BPV, hence light-induced piezoelectricity. Therefore, further investigations are needed on thin films to overcome such a limit for light-induced piezoelectricity enhancement for potential device implementation at the nanoscale.

Here, we show a pathway for dynamic control of enhanced piezoelectricity under illumination in a BFO/DyScO₃ (DSO) thin film by implementation of an in-plane geometry. We performed piezoresponse force microscopy (PFM) and conductive atomic

**ADVANCED
SCIENCE NEWS**

www.advancedsciencenews.com

**ADVANCED
ELECTRONIC
MATERIALS**

www.advelectronicmat.de

force microscopy (C-AFM) based measurements under illumination, revealing a locally enhanced piezoelectric signal depending on the in-plane electrode distance, and domain wall (DW) orientation due to their influence on the photocurrent and open circuit voltage from the BPV effect. Moreover, we show dynamic control of piezoelectric signals with their sinusoidal behavior closely linked to the photocurrent variations under polarization-resolved illumination, further proving that modulation of the BPV effect is the key control parameter. Temporal decay measurements show persistent piezoelectric signals associated with the trapping of photoinduced charges. These results establish the framework for dynamic control of piezoelectricity enhancement in a thin film via modulation of the BPV effect, offering its potential for applications in nano-optoelectronic devices.

2. Results and Discussion

A series of epitaxial BFO thin films were prepared to explore light-induced piezoelectricity enhancement, using different combinations: BFO on insulating substrates, such as DSO and TbScO$_3$ (TSO); BFO with a bottom electrode SrRuO$_3$ (SRO) on TSO; and BFO on an oxygen deficient substrate, SrTiO$_{3-d}$ (STO). Details of the film structures and conditions characterized by X-ray diffraction are provided in the Supporting Information (Figure S1, Supporting Information). For the films with the insulating substrate and no bottom electrode, top gold electrodes were deposited and grounded by a needle contact, enabling an in-plane geometry operation between the tip and the top electrode. Ferroelectric domain structures of a BFO/DSO film were imaged by out-of-plane (OOP) and in-plane (IP) PFM phase scans at room temperature in dark, as shown in **Figure 1**. As can be seen, the OOP phase image shows almost uniform contrast, pointing in one direction, while the IP phase image shows stripe domains with a width of ≈150 nm, revealing the typical 71° domain configurations.[24] The schematic shows the crystal orientation and the polarization directions alternating between $[\bar{1}11]_{pc}$ and $[111]_{pc}$ directions, resulting in in-plane net polarization, P^{net}. To investigate light-induced enhancement, using the photoelectric AFM setup (see Figure S2, Supporting Information for the details), local OOP PFM amplitude signals are measured by increasing the photon flux, Φ up to 1.3×10^{19} cm^{-2} s^{-1}, as shown in Figure 1c. We note that all of the PFM amplitude signals under illumination are rescaled by dividing them by the pristine signal (no illumination), indicating multipliers for enhancement, and also analyzed with Pearson correlation coefficients and t-test function for statistical insights (see Statistical Analysis section and Supporting Information for details). As a result, Figure 1c shows a characteristic evolution of the amplitude signal, first sharply increasing from the pristine value (up to $\Phi = 2.5 \times 10^{18}$ cm^{-2} s^{-1}), and then gradually increasing to result in a saturation-like state, eventually revealing almost a sixfold enhancement of the PFM amplitude signal ($\Phi = 1.3 \times 10^{19}$ cm^{-2} s^{-1}). Given that the excitation ac voltage, V_{ac} used to measure the PFM amplitude signal is 1 V, and thus the measured PFM amplitude signal is directly proportional to the surface displacement, the effective piezoelectric coefficient, d_{zz} is also found to show almost a sixfold increase, as a result of light-induced piezoelectricity enhancement. (for details, see

the section on analysis of d_{zz} and Figure S3, Supporting Information). Importantly, the same measurements on BFO/TSO show the same enhancement behavior, but the other BFO thin films with a bottom electrode (BFO/SRO/TSO) or conducting interfaces (BFO/STO) did not show such light-induced piezoelectricity enhancement due to the insufficient effective length of the material, being the film thickness of ≈200 nm. This can be explained by the recent model proposed for the realization of light-induced piezoelectricity enhancement in bulk BFO,[21] revealing the critical role of effective material length. The surface displacement generating the PFM amplitude signals are:[25,26]

$$D = D_{piezo} + D_{electrostatic} \tag{1}$$

Which can be detailed further to:

$$D = d_{zz} V_{ac} + \frac{C'}{k^*}(V_{dc} - V_{sp})V_{ac} \tag{2}$$

where d_{zz} is the effective OOP piezoelectric coefficient, $C' = \frac{dC}{dz}$ is the derivative of the tip capacitance in the z-direction, k^* is the effective contact elastic stiffness, and V_{sp} is the surface potential. Under illumination, the BPV effect generates a local potential related to the open circuit voltage, V_{oc}, which in this case dominates the V_{sp}. Under this assumption, the total displacement would be rearranged as:

$$D = \left(d_{zz} - \frac{C'}{k^*}V_{oc}\right)V_{ac} \tag{3}$$

According to Sturman and Fridkin,[27] the V_{oc} is given by:

$$V_{oc} = -\frac{J}{(\sigma_d + \sigma_{ph})}l \tag{4}$$

where J is the BPV current, σ_d and σ_{ph} are the dark- and photoconductivity respectively, and l is the effective device length. Therefore, the implementation of in-plane geometry without a bottom electrode or conducting interface for the thin film can provide the critical length regime to produce sufficient open circuit voltages for light-induced piezoelectricity enhancement.

To verify this role of the in-plane length, we performed a series of electrode distance (by moving the AFM-tip away) dependent measurements of local OOP PFM amplitude signals. First, the evolution of the rescaled PFM amplitude signals under illumination in two locations with different electrode distances is shown in **Figure 2**a. Throughout these measurements with electrode distances, the focus of laser light is under the AFM tip. Note that the evolution of PFM amplitude signals is equivalent to the evolution of d_{zz}, provided that V_{ac} is 1 V, as previously mentioned. The inset describes the electrode distance by moving the AFM-tip away from it. Clear differences in enhancement are seen such that the rescaled amplitude signal ($=d_{zz}$) of the location with the shortest electrode distance (57 μm) is found to show more than a fourfold increase, whereas that of location with the furthest electrode distance (488 μm) results in almost an eightfold enhancement. This indicates clear dependence of the enhancement on the in-plane
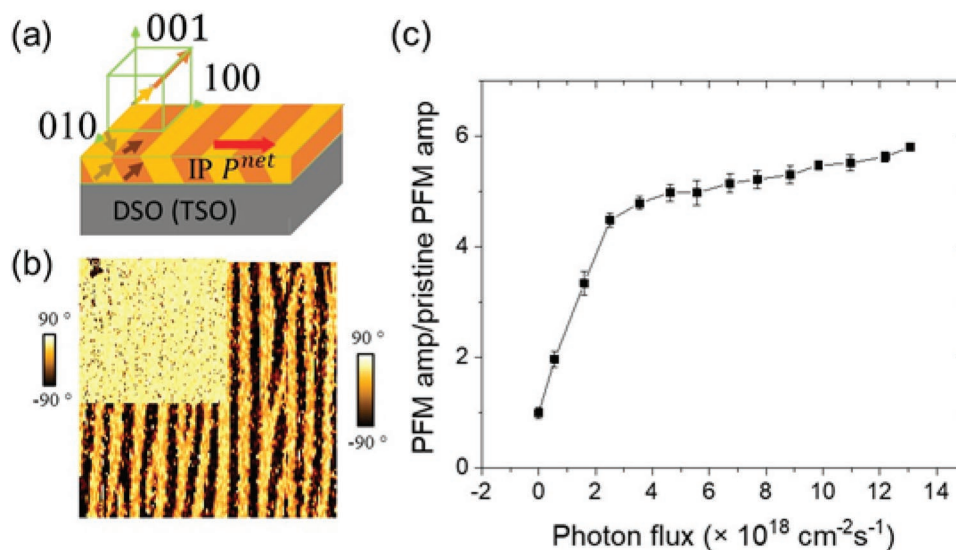
**ADVANCED
SCIENCE NEWS**

www.advancedsciencenews.com

**ADVANCED
ELECTRONIC
MATERIALS**

www.advelectronicmat.de

Figure 1. Light-induced piezoelectricity by implementation of in-plane geometry in a BFO thin film. a) Schematic of the in-plane film geometry for BFO with the resultant net polarization, P_{net} along the IP projection of two polarization variants along the $[\bar{1}11]_{pc}$ and $[111]_{pc}$ directions. b) IP and OOP (inset) PFM phase images of the BFO sample. c) Evolution of the rescaled OOP PFM amplitude signals with increasing the photon flux.
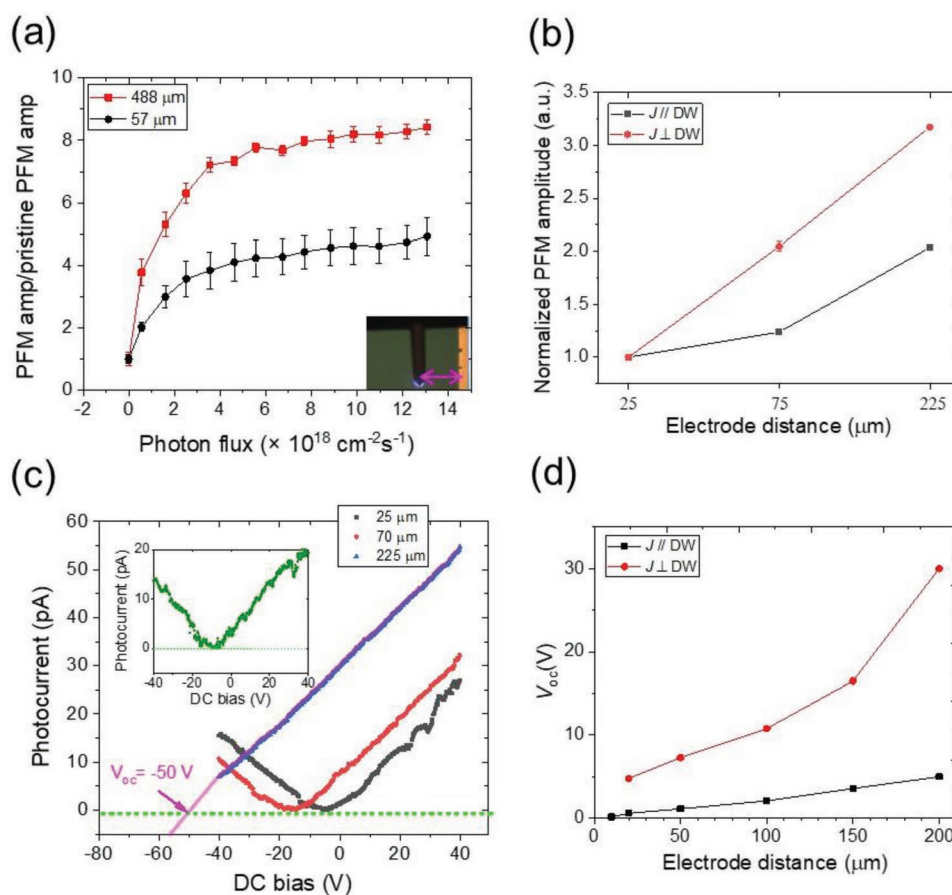

Figure 2. Further enhancement of piezoelectricity via modulation of the BPV through electrode distances and DW orientations. a) Electrode distance dependent enhancement of the rescaled OOP PFM amplitude signals with increasing the photon flux. b) Enhancement of the rescaled OOP PFM amplitude signals by increasing the electrode distance under illumination with the constant photon flux of 2×10^{19} cm^{-2} s^{-1}. c) Representative C-AFM based spectroscopic I–V curves for electrode distance dependent V_{oc} along the J⊥DW direction. The inset shows the I–V curve for the furthest electrode distance of 225 µm under the J//DW condition. d) Electrode distance dependent V_{oc} measured in macroscopic in-plane geometry.

**ADVANCED
SCIENCE NEWS**
www.advancedsciencenews.com

**ADVANCED
ELECTRONIC
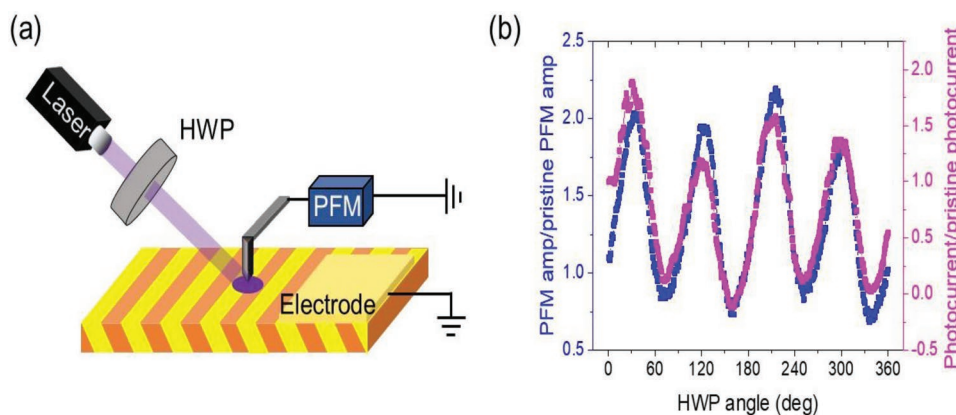MATERIALS**
www.advelectronicmat.de

Figure 3. Dynamic control of piezoelectricity enhancement via light polarization. a) Schematic of light polarization dependent PFM (C-AFM) measurements by implementation of the half wave plate (HWP). b) The representative measurement on the electrode location of 225 µm along the J//DW direction of the rescaled PFM amplitude and photocurrent signals dependent on light polarization angles with a constant photon flux of 2×10^{19} cm^{-2} s^{-1}. Note that the pristine PFM amplitude and photocurrent values are obtained before operating rotation of the light polarization angle.

length which should be associated with photovoltages due to the BPV effect. For more detailed analysis, the rescaled local PFM amplitudes are also measured under smaller increasing distance scales with the constant photon flux of 2×10^{19} cm^{-2} s^{-1}, as shown in Figure 2b, clearly revealing the increasing trend of light-induced piezoelectricity enhancement along with the increased in-plane length. Further, we investigated DW orientation dependence of enhanced piezoelectricity under illumination along distant locations by increasing electrode distances along two directions, defined by their associated photocurrent (J) directions parallel (J//DW) and normal (J⊥DW) to the DWs. As a result, the rescaled PFM amplitude signals qualitatively show larger light-induced enhancement at the furthest distance location (225 µm) along the J⊥DW direction than in the J//DW direction with a threefold and twofold increase from their value at the nearest (25 µm) location respectively. This implies the effect of DWs on the BPV effect, eventually affecting the light-induced piezoelectricity enhancement. For deeper insights into its link with the BPV effect, particularly on the role of the open circuit voltage (V_{oc}), C-AFM based spectroscopic I–V curves with the constant photon flux of 2×10^{19} cm^{-2} s^{-1} are measured, as seen in Figure 2c. Clearly, the V_{oc} along the J⊥DW direction is found to increase nearly proportionally with the electrode distance from −4.7 V (25 µm) to −16.1 V (70 µm) and eventually −50 V (225 µm). On the other hand, the V_{oc} along the J//DW direction show a measurable value of −8.2 V only at the furthest electrode distance (225 µm), as shown in the inset. For more reliable and accurate investigations, macroscopic photovoltaic measurements were performed on a sample patterned by photolithography with precise electrode spacing from 10 to 200 µm. As shown in Figure 2d, the V_{oc} is essentially found to be proportionally increasing with the increased electrode distance, further proving the role of effective in-plane material length on the generation of an internal electric field in the film. In addition, the V_{oc} is also found to be clearly dependent on the DW orientation, such that it is more largely increased in the case of J⊥DW than that of J//DW. This can be explained by the previous photoconductivity-driven study with the two resistance model,[24] pointing to higher effective resistance and thus lower

conductivities for the case of J⊥DW, consequently resulting in a higher V_{oc}.

Given that piezoelectricity can be further enhanced via tuning of the BPV, we can also dynamically control it by varying light polarization using a half-wave plate (HWP), as schematically shown in **Figure 3**a. According to the following BPV effect equation, the photocurrent, J_i along the i-th direction in the film:[27]

$$J_i = I_0 \beta_{ijk} \left(e_j e_k^* + e_k e_j^* \right) \quad (5)$$

where I_0 is the light intensity, $\beta_{ijk} = \beta_{ikj}$ is a third-order tensor bearing the same symmetry as the piezoelectric tensor and describing the linear photocurrent, e is the unit polarization vector of light, and e^* is its conjugate vector. Due to the symmetric properties, the β_{ijk} tensor could be transferred into the form of a 3×6 tensor β_{ij}. The tensor β_{ij} differs from zero only in the case of a non-centrosymmetric media. For a C_{3v} point group symmetry, to which BFO belongs, the number of independent nonzero components of the β_{ij} tensor is four.[27] The photocurrents perpendicular and parallel to the in-plane projection of crystallographic directions along the $[111]_{pc}$ or $[\overline{1}11]_{pc}$ axis of BFO are of interest here. Therefore, we define directions of the photocurrent, according to the in-plane projection of the crystallographic direction, which is the same as the direction of P^{net}. According to the phenomenological theory, the photocurrents of both monodomain and stripe domain thin films can be expressed in a simple form as the following:[24]

$$J_\perp = A_\perp \sin(4\theta) + Off_\perp \quad (6)$$

$$J_{//} = A_{//} \cos(4\theta) + Off_{//} \quad (7)$$

where $J_\perp$ and $J_{//}$ are the photocurrents collected perpendicular and parallel to the direction of P^{net} respectively, $A_\perp$ and $A_{//}$ are the photocurrent amplitudes of sin (4θ) and cos (4θ) dependencies for $J_\perp$ and $J_{//}$ respectively, and $Off_\perp$ and $Off_{//}$ are the photocurrent offsets independent of the light polarization.
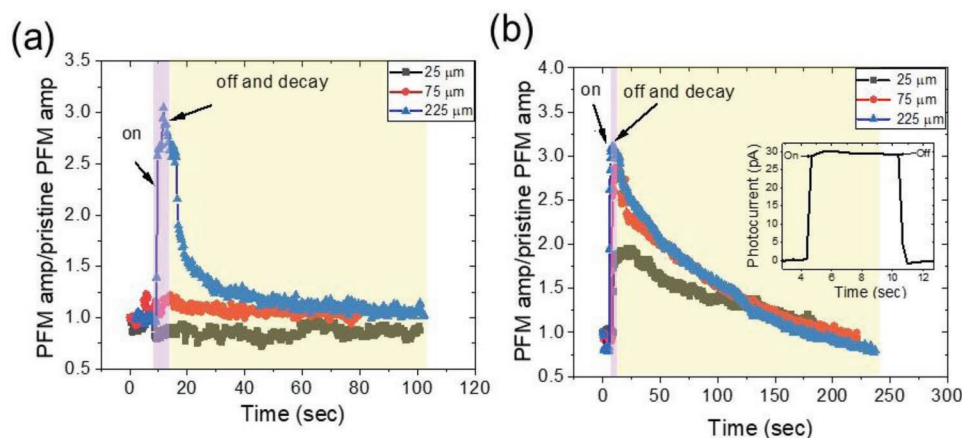
Figure 4. Decay of piezoelectricity enhancement via photoconductivity. Temporal decay of the rescaled PFM amplitude signals dependent on electrode distances along the a) J//DW direction and b) the J⊥DW direction. Inlet shows the representative decay of photocurrent signals for the electrode distance of 225 μm along the J⊥DW direction. These measurement data are obtained by switching on and off the laser with the constant photon flux of 2×10^{19} cm^{-2} s^{-1}.

Consequently, the V_{oc} from Equation (4) is also associated with such photocurrent variations due to the light polarization, depending on $J_\perp$ and $J_{//}$:

$$V_{oc} \text{ for } J_\perp = -\frac{A_\perp \sin(4\theta) + Off_\perp}{(\sigma_d + \sigma_{ph})} l \qquad (8)$$

$$V_{oc} \text{ for } J_{//} = -\frac{A_{//} \cos(4\theta) + Off_{//}}{(\sigma_d + \sigma_{ph})} l \qquad (9)$$

As shown in Figure 3b, for the representative measurement on the electrode location of 225 μm along the J//DW direction, the rescaled OOP PFM amplitude signals show dynamics of their sinusoidal evolution induced by light polarization, spanning over a large range of values under illumination with the constant photon flux of 2×10^{19} cm^{-2} s^{-1}. This reveals the impact of polarization angle, leading to a further threefold enhancement of the PFM amplitude signal, in addition to the already enhanced signal induced by light. Moreover, dynamics of the rescaled photocurrent variations are shown, also revealing their sinusoidal behavior with the same trend as the PFM amplitude, indicating their correlation with a linear relationship. The same trend of the correlation between the PFM amplitude and photocurrent signals is seen for the case of electrode location of 225 μm along the J⊥DW direction, as shown in Figure S4, Supporting Information.

Because the presence of the tunable BPV effect is the critical control parameter for the realization of light-induced piezoelectricity enhancement, further insights into its time-dependent behavior will provide a deeper understanding of optoelectronic properties. For this, we performed temporal decay measurements of enhanced OOP PFM amplitude (rescaled) signals along the J//DW and J⊥DW (**Figure 4**a and 4b respectively) directions by switching on and off the laser for the constant photon flux of 2×10^{19} cm^{-2} s^{-1}. In the case of J//DW (Figure 4a), as expected from Figure 2b, the enhanced PFM amplitude signal by switching on the laser is rather small for the electrode distance of 25 and 75 μm with nearly zero generated V_{oc}.

Nevertheless, the V_{oc} is sufficiently large for the electrode distance of 225 μm. Interestingly, after removing illumination, the enhanced amplitude signal is not instantaneously decreased to its pristine value, showing exponential decay over a duration of 100 s. In addition, the resultant amplitude signal after switching off the laser for 100 s, is still higher than the pristine value, showing persistent behavior of the enhanced piezoelectricity. In the case of J⊥DW (Figure 4b), the enhanced PFM amplitude signals are clearly seen with a proportionally increasing trend along with a larger electrode distance. After switching off the light, all these enhanced amplitude signals show exponentially decaying behavior over 200 s, reaching close to the pristine values before switching on the light. Importantly, we note that the photocurrent signals are rapidly reduced to zero within a few milliseconds, after switching off the light, as seen in the inlet of Figure 4b. However, the long-lived and exponential decay of PFM amplitude signals resembles the behavior of persistent photoconductivity as previously reported,[28] due to the role of trapped photocarriers. Based on this, we use the following model to explain the decay behavior of enhanced PFM amplitude signals along both J⊥DW and J//DW directions, as supported by the two-step fitting in Figure S5, Supporting Information.

$$PFM_{amp}(t) = PFM_{amp}(0) + A_1 e^{(-t)/\tau_1} + A_2 e^{(-t)/\tau_2} \qquad (10)$$

where $PFM_{amp}(t)$ is the PFM amplitude signal at a specific time, $PFM_{amp}(0)$ is the pristine PFM amplitude signal, t is the measuring time, A_1 and A_1 are the conductivity-related parameters, τ_1 and τ_2 are the decay time occurring over two steps (usually τ_1 refers to a direct recombination time, and τ_2 refers to the time of re-emitted carriers from trapping levels).[29] As a result of fitting this model (see Figure S5, Supporting Information for the details), we found for J⊥DW that τ_1 and τ_2 are ≈5.4 and 306 s respectively, and for J//DW that τ_1 and τ_2 are ≈6.5 and 123 s respectively. These values are several orders of magnitude higher than the usual carrier lifetime on the order of several microseconds.[29] Under illumination, the photoinduced charge carriers initially reach an equilibrium state and fill the levels located under the Fermi level.[28,30] After switching

**ADVANCED
SCIENCE NEWS**

www.advancedsciencenews.com

**ADVANCED
ELECTRONIC
MATERIALS**

www.advelectronicmat.de

off the light, apart from the direct recombination process, the trapped charge carriers are gradually re-emitted, leading to the prolonged decay time through a de-trapping process. This should be responsible for the persistent behavior of enhanced PFM amplitude signals. In the case of J⊥DW, as discussed by the two resistance models before,[24] generation of higher V_{oc} than the case of J//DW should further boost trapping of photoinduced charge carriers in sub-levels, thus allowing for longer survival of piezoelectricity enhancement.

3. Conclusions

In summary, we show a pathway for light-induced piezoelectricity enhancement by implementing an in-plane geometry of a BFO thin film, allowing for modulation of the BPV effect. Controlling the in-plane distance between the AFM tip and the electrode position, an eightfold enhancement of the pristine OOP PFM amplitude signal ($=d_{zz}$) is achieved, revealing the key role of effective material length for sufficient realization of the BPV effect. We also show the dependence of piezoelectricity enhancement on the DW orientations, revealing higher enhancement in the case of J⊥DW than J//DW, due to its larger V_{oc} values. Dynamic control of piezoelectricity with sinusoidal behavior is seen by control of light polarization, revealing another threefold enhancement, in addition to the already existing enhanced signal induced by light. Moreover, temporal decay measurements of enhanced piezoelectric signals under illumination show exponential decay, dependent on electrode distances and DW orientations, revealing the mechanism behind should be linked to trapping of photocarriers in sub-levels. These results establish a framework of light-induced piezoelectricity for BFO thin films, offering promising directions of ferroelectric thin films for multifunctional nano-optoelectronic devices.

4. Experimental Section

Sample Preparations: DyScO$_3$ (DSO) and TbScO$_3$ (TSO) single crystal substrates (SurfaceNet GmbH) were annealed in the oxygen-rich environment at 1050 °C for 2 h before loading in the pulsed laser deposition (PLD) chamber. Stripe domain BFO/DSO and BFO/TSO thin films with 71° DW patterns were grown on the bare (110)-oriented DSO and (110)-oriented TSO substrate respectively. BFO/DSO and BFO/TSO were deposited at 650 °C under an oxygen pressure of 0.15 mbar, and the pulse laser energy was set at 0.43 J cm^{-2} with a 10 Hz frequency. All the stripe domain thin films were ≈300 nm thick. A 10–15 nm thick bottom electrode SrRuO$_3$ (SRO) was used in BFO/SRO/TSO thin film fabrication. The SRO layer was deposited under an oxygen pressure of 0.20 mbar, and the pulse laser energy was set at 0.43 J cm^{-2} with a 5 Hz frequency. For BFO/STO, monodomains were grown on the STO (001)-oriented 4° miscut substrate with the deposition at 650 °C under an oxygen pressure of 0.15 mbar, and the pulse laser energy was set at 0.43 J cm^{-2} with a 10 Hz frequency. For oxygen deficiency, the BFO/STO samples were annealed at high temperatures in an 80% N_2 + 15% Ar_2 + 5% H_2 atmosphere. Further details of the BFO/STO growth and treatment conditions can be found in the recently published report.[30]

Top Electrode Fabrication: Classical photolithography process was used to structure rectangular DC sputtered ≈60 nm Au electrode pairs (900 × 600 µm) on the top of BFO thin films. The spacing of the electrode pairs was ranging from 10 to 200 µm.

PFM and C-AFM under Illumination: XE-100 Park AFM system was used for local AFM/PFM investigations. A 405-nm laser source (Newport LQA405-85E) focused into an ellipsoidal spot area of ≈0.33 mm × 0.29 mm was used for illumination. PFM was run with an ac bias of 1–2 V with a frequency of 22.36 kHz applied on the conductive tip (PPP-EFM from Nanosensors). For steady-state conditions, the PFM signals were detected after a few seconds, so that the system was always in the quasi-steady state and mitigating any parasitic effect such as laser-induced heating. For C-AFM-based local photocurrent measurements, the same XE-100 Park AFM system equipped with a trans-impedance amplifier (Femto, DLPCA-200) and filter (Stanford Research Systems, SR560) was used. The currents/photocurrents detected by the conductive tip were measured through the amplifier with a typical gain of 10^8. The voltage was further ten times amplified and filtered with a low-pass filter with typical cut-off frequency of 100 Hz and 12 dB. For light polarization dependent measurements, the HWP was used for varying the angle between the current direction and the polarization axis of the light.

Macroscopic Photoconductivity Measurements: The optoelectronic measurements were run in a Janis cryostat under the illumination of a polarised 405 nm laser (3.06 eV) with a power of 40 mW. A high impedance electrometer (Keithley 6517B) was used to collect the data.

Statistical Analysis: To show reliable trend of the data sets, mean values were shown by using average values of the measurement data (the sum of all the values over the number of data) with error bars calculated by first obtaining the standard deviation, $\sigma = \sqrt{\frac{\sum_{i=1}^{n}(x_i - \bar{x})^2}{n-1}}$, where n is the number of data, x_i is each data value, and $\bar{x}$ is the mean of data values, and then using the standard error equation, $SE = \frac{\sigma}{\sqrt{n}}$. The number of measurement data for each statistical analysis was 5, for Figures 1c and 2a,b. For evaluation of significant differences between the data values, two types of calculations were used: the Pearson correlation coefficients and the t-test function with one-tailed testing (For details and calculation results, see Supporting Information). The software programs used in these analyses and plotting were Excel and Origin.

Supporting Information

Supporting Information is available from the Wiley Online Library or from the author.

Conflict of Interest

The authors declare no conflict of interest.

Author Contributions

Y.H. and H.Z. contributed equally to this work. Y.H. and M.A. conceived the project. Y.H. and H.Z. designed the experiments. H.Z. fabricated the BFO thin films and performed macroscopic photovoltaic measurements between the top electrodes. Y.H. performed PFM, C-AFM, spectroscopy, and light polarization dependent measurements under illumination. Y.H., H.Z., and M.A. co-wrote the paper. Y.H., H.Z., and M.A. acknowledge

ADVANCED
SCIENCE NEWS
www.advancedsciencenews.com

ADVANCED
ELECTRONIC
MATERIALS
www.advelectronicmat.de

D. Walker in the Department of Physics, University of Warwick for his supporting X-ray diffraction measurements during this work.

[1] R. J. Zeches, M. D. Rossell, J. X. Zhang, A. J. Hatt, Q. He, C.-H. Yang, A. Kumar, C. H. Wang, A. Melville, C. Adamo, G. Sheng, Y.-H. Chu, J. F. Ihlefeld, R. Erni, C. Ederer, V. Gopalan, L. Q. Chen, D. G. Schlom, N. A. Spaldin, L. W. Martin, R. Ramesh, *Science* **2009**, *326*, 977.

[2] C. H. Yang, J. Seidel, S. Y. Kim, P. B. Rossen, P. Yu, M. Gajek, Y. H. Chu, L. W. Martin, M. B. Holcomb, Q. He, P. Maksymovych, N. Balke, S. V. Kalinin, A. P. Baddorf, S. R. Basu, M. L. Scullin, R. Ramesh, *Nat. Mater.* **2009**, *8*, 485.

[3] K. J. Choi, M. Biegalski, Y. L. Li, A. Sharan, J. Schubert, R. Uecker, P. Reiche, Y. B. Chen, X. Q. Pan, V. Gopalan, L.-Q. Chen, D. G. Schlom, C. B. Eom, *Science* **2004**, *306*, 1005.

[4] L. W. Martin, Y. H. Chu, R. Ramesh, *Mater. Sci. Eng., R* **2010**, *68*, 89.

[5] H. Y. Hwang, S. W. Cheong, P. G. Radaelli, M. Marezio, B. Batlogg, *Phys. Rev. Lett.* **1995**, *75*, 914.

[6] H. N. Lee, D. Hesse, N. Zakharov, U. Gösele, *Science* **2002**, *296*, 2006.

[7] O. Paull, C. Xu, X. Cheng, Y. Zhang, B. Xu, K. P. Kelley, A. de Marco, R. K. Vasudevan, L. Bellaiche, V. Nagarajan, D. Sando, *Nat. Mater.* **2022**, *21*, 74.

[8] J. X. Zhang, B. Xiang, Q. He, J. Seidel, R. J. Zeches, P. Yu, S. Y. Yang, C. H. Wang, Y. H. Chu, L. W. Martin, A. M. Minor, R. Ramesh, *Nat. Nanotechnol.* **2011**, *6*, 98.

[9] L. You, Z. Chen, X. Zou, H. Ding, W. Chen, L. Chen, G. Yuan, J. Wang, *ACS Nano* **2012**, *6*, 5388.

[10] J. H. Lee, K. Chu, A. A. Ünal, S. Valencia, F. Kronast, S. Kowarik, J. Seidel, C.-H. Yang, *Phys. Rev. B* **2014**, *89*, 140101.

[11] M. Zhang, X. Zhang, X. Qi, H. Zhu, Y. Li, Y. Gu, *Ceram. Int.* **2018**, *44*, 21269.

[12] J. Seidel, M. Trassin, Y. Zhang, P. Maksymovych, T. Uhlig, P. Milde, D. Köhler, A. P. Baddorf, S. V. Kalinin, L. M. Eng, X. Pan, R. Ramesh, *Adv. Mater.* **2014**, *26*, 4376.

[13] Y. Heo, J. Hong Lee, L. Xie, X. Pan, C.-H. Yang, J. Seidel, *NPG Asia Mater* **2016**, *8*, e297.

[14] P. Sharma, Y. Heo, B.-K. Jang, Y. Liu, V. Nagarajan, J. Li, C.-H. Yang, J. Seidel, *Adv. Mater. Interfaces* **2016**, *3*, 1600033.

[15] P. Sharma, Y. Heo, B. K. Jang, Y. Y. Liu, J. Y. Li, C. H. Yang, J. Seidel, *Sci. Rep.* **2016**, *6*, 32347.

[16] K. Chu, B.-K. Jang, J. H. Sung, Y. A. Shin, E.-S. Lee, K. Song, J. H. Lee, C.-S. Woo, S. J. Kim, S.-Y. Choi, T. Y. Koo, Y.-H. Kim, S.-H. Oh, M.-H. Jo, C.-H. Yang, *Nat. Nanotechnol.* **2015**, *10*, 972.

[17] M.-M. Yang, A. N. Iqbal, J. J. P. Peters, A. M. Sanchez, M. Alexe, *Nat. Commun.* **2019**, *10*, 2791.

[18] Y. Heo, B.-K. Jang, S. J. Kim, C.-H. Yang, J. Seidel, *Adv. Mater.* **2014**, *26*, 7568.

[19] Y. Heo, S. Hu, P. Sharma, K.-E. Kim, B.-K. Jang, C. Cazorla, C.-H. Yang, J. Seidel, *ACS Nano* **2017**, *11*, 2805.

[20] Y. Heo, P. Sharma, Y. Y. Liu, J. Y. Li, J. Seidel, *J. Mater. Chem. C* **2019**, *7*, 12441.

[21] Y. Heo, M. Alexe, *Adv. Mater.* **2022**, *34*, 2105845.

[22] M. Nakamura, S. Horiuchi, F. Kagawa, N. Ogawa, T. Kurumaji, Y. Tokura, M. Kawasaki, *Nat. Commun.* **2017**, *8*, 281.

[23] Y. Zhang, T. Holder, H. Ishizuka, F. de Juan, N. Nagaosa, C. Felser, B. Yan, *Nat. Commun.* **2019**, *10*, 3783.

[24] A. Bhatnagar, A. Roy Chaudhuri, Y. Heon Kim, D. Hesse, M. Alexe, *Nat. Commun.* **2013**, *4*, 2835.

[25] R. K. Vasudevan, N. Balke, P. Maksymovych, S. Jesse, S. V. Kalinin, *Appl. Phys. Rev.* **2017**, *4*, 021302.

[26] J. W. Hong, S.-I. Park, Z. G. Khim, *Rev. Sci. Instrum.* **1999**, *70*, 1735.

[27] B. Sturman, V. Fridkin, *The Photovoltaic and Photorefractive Effects in Noncentrosymmetric Materials*, Routledge, London **2021**, p. 264.

[28] A. Bhatnagar, Y. H. Kim, D. Hesse, M. Alexe, *Nano Lett.* **2014**, *14*, 5224.

[29] M. Alexe, *Nano Lett.* **2012**, *12*, 2193.

[30] H.-B. Zhang, M. Alexe, *Adv. Electron. Mater.* **2022**, *8*, 2100665.